Polarizability, Stark shifts, and field ionization of highly charged ions in ultraintense lasers

Evan C. Jones, Zachery P. Andreula, and Barry C. Walker ** Department of Physics and Astronomy, University of Delaware, Newark, Delaware 19716, USA

(Received 14 October 2022; accepted 31 January 2023; published 6 March 2023)

We have calculated the polarization and Stark-shifted binding energy for ultraintense lasers interacting with highly charged ions across the periodic table from beryllium to uranium at intensities up to 10^{22} W cm⁻². The induced dipole and Stark shifts for the bound states can be as large as $0.1ea_0$ and $50E_h$. Calculations of tunneling show the impacts of polarization and Stark shifts on the ionization rate are significant but counteracting. The work resolves a long-standing question of how field-free derivations of the tunneling response for highly charged ions have been quantitatively successful in relativistic, ultrahigh-intensity experiments. Using a scaling relationship, the results can be generalized to give the induced electric dipole for any species across an intensity range from 10^{15} to 10^{22} W cm⁻².

DOI: 10.1103/PhysRevA.107.033102

I. INTRODUCTION

Due to the advancement of chirped pulse amplification [1] laser intensities now exceed 10^{23} W cm⁻² [2], corresponding to electric fields reaching $1500E_he^{-1}a_0^{-1}$ in atomic units (where E_h is Hartree energy, e is the elementary charge, and a_0 is the Bohr distance). There are more than 100 laser facilities across the world that can now deliver laser pulses with a peak power of more than a petawatt [3]. At high intensities, the electrons bound to the ions are no longer in a "fieldfree" environment. Atomic ionization studies at intensities of 10¹⁹ W cm⁻² have reported charge states as high as Xe²⁶⁺ [4,5]. The effects of the laser magnetic field and electron spin [6–9] in ultrastrong fields have been theoretically quantified [10,11]. The Stark shift has been well studied for high-lying states of atoms and molecules in strong fields [12,13] but is coming into focus as being important for lower-lying and ground states [14-16] as well as states of condensed-matter systems [17].

In this work, we characterize the net impact of intensities generated by terawatt [18,19] and petawatt [20] laser systems on both the polarization and Stark shift of bound states in highly charged ions. We consider species across the periodic table from beryllium to uranium. As an application of the fundamental response, the tunneling-ionization rates from the polarized and Stark-shifted species are reported. An interplay between polarization and the Stark shift resolves how models based on a field-free approximation can appear to agree with experimental measurements [5,21–25] when, in fact, the atomic states are shifted and polarized in the field.

To introduce how fields change atomic states we examine the response of krypton [23]. In Fig. 1 the outermost-electron wave function of Kr^{25+} is shown at an intensity of 5 × 10¹⁸ W cm⁻². The outermost electron is often identified as spherically symmetric, hydrogenic 3s about a closed-shell neon $1s^22s^22p^6$ core. We choose $5 \times 10^{18} \text{ W cm}^{-2}$ because it corresponds to an intensity that is one half of the "barriersuppression ionization" (BSI), or "classical ionization," of the outermost electron of Kr²⁵⁺. High-field interactions are very nonlinear; an order of magnitude change in the intensity can change the amount of ionization by 10 orders of magnitude [26,27]. Modern experiments have an intensity range from a few percent of BSI up to BSI.

In Fig. 1(a) one can see the outermost-electron wave function $|\psi(x,0,z)|$ in the plane of the electric field $\vec{E} =$ $12.4E_he^{-1}a_0^{-1}\hat{z}$. The force from the external field causes the electron to spatially displace away from the nucleus. Figure 1(b) is a plot of $\psi(z)^*\psi(z)$ with no external field and in a field that is 71% of the BSI field (i.e., one half of the BSI intensity). The shift of the peak electron probability to $z \approx -0.4a_0$ is identifiable in Fig. 1(b) and evaluates to a similarly large electric dipole $\vec{p} = 0.33ea_0\hat{z}$. The binding atomic potential for the outer electron with and without the external field is also plotted in Fig. 1(b) as a function of the distance from the nucleus along the electric field (z axis).

The Stark shift due to polarized state alignment in the external field can be a sizable fraction of the binding energy since $|\vec{p}| \sim 0.1ea_0$ and ultrastrong fields are of the of order 10 to $10^2 E_h e^{-1} a_0^{-1}$. In Fig. 1(b) the Stark shift of the binding energy from $-42.2E_h$ to $-45.1E_h$ is displayed in the potentials as an offset of the electron wave-function probability $\psi(z)^*\psi(z)$. The results in Fig. 1 were calculated according to the method described in Sec. II.

For introductory purposes, we briefly describe ionization and polarizability for highly charged ions. When the laser field is comparable to the atomic Coulomb field, an effective potential barrier is created through which the electrons tunnel ionize [28,29]. In Fig. 1(b) the effective laser and Coulomb potential barrier through which Kr²⁵⁺ tunnel ionizes is located in the range $-3a_0 < z < -0.75a_0$. The tunneling time under the barrier [30–32] is impacted by the polarization and Stark shift of the tunneling electron.

Tunneling ionization is commonly described with a model derived by Ammosov, Delone, and Krainov (ADK) [33],

^{*}Corresponding author: bcwalker@udel.edu

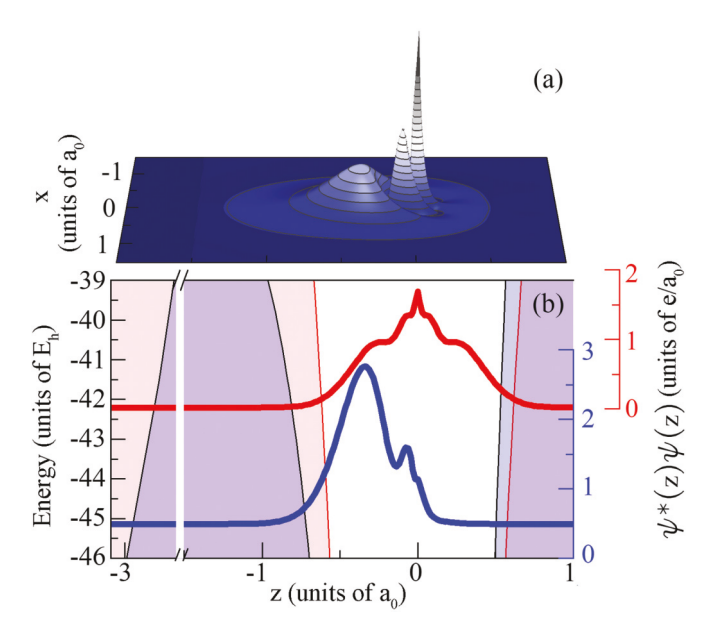


FIG. 1. (a) Wave-function magnitude $|\psi(x,0,z)|$ in the y=0 plane for the Kr^{25+} outermost electron in an external electric field (intensity) of $12.4E_he^{-1}a_0^{-1}\hat{z}$ (5.4 × 10^{18} W cm⁻²). (b) The electron probability $\psi(z)^*\psi(z)$ is shown field free (red upper thick line) and along the $12.4E_he^{-1}a_0^{-1}\hat{z}$ field direction (blue lower thick line). The $\psi(z)^*\psi(z)$ probability (right y axis) is offset to indicate the binding energy of $-42.2E_h$ with no field and $-45.1E_h$ in the field. The binding ion potentials for the Kr^{25+} outermost electron ion with no external field (red thin line, light fill to the x axis) and in an electric field of $12.4E_he^{-1}a_0^{-1}\hat{z}$ (black thin line, dark fill to the x axis) are also shown in (b).

which will be discussed in depth in the Sec. IV. For the moment, Fig. 2(a) depicts the ion charge-state probability of krypton due to field ionization as a function of the laser intensity for a single cycle of $\lambda=800$ nm light calculated using the ADK model. One can see a single electron from ground-state krypton is ionized at 10^{14} W cm⁻². The sequential field-ionization process continues with increasing intensity over 10 orders of magnitude until the last "1s" electron is field ionized at 10^{24} W cm⁻², leaving a bare Kr³⁶⁺ nucleus. Gaps in the ionization potential, such as the ones that occur across

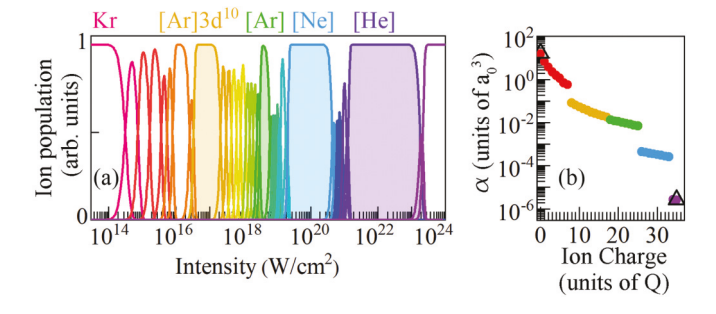


FIG. 2. (a) Krypton ion population as a function of the intensity for a single cycle of 800-nm radiation. The electron configuration for selected ionization steps is indicated above the graph. (b) The semiempirical polarizability α for krypton as a function of the ion charge with the symbol spectral value tied to the ionization in (a). The experimental α values for neutral Kr and the calculated one-electron 1s state (black open triangle) are included.

electron shells, are seen in Fig. 2(a) with the core identified above the ion population in that intensity region.

While the above ionization response focuses on the photoelectron in the continuum, the strong external field also polarizes the initial bound state for the electron of the highly charged ion. The homogeneous polarizability model $\alpha = |\vec{p}|/|\vec{E}|$ approximates [34] highly charged ions as a sphere with $\alpha = Kr^3$, where r is the atomic radius of the outermost electron and K is a factor accounting for the radial structure in an atom with an atomic number of Z. Using the experimentally measured neutral atom polarizability and the calculated hydrogenic quantum 1s polarizability as end-point requirements for K gives the approximate weak-field polarizability in atomic units as

$$\alpha = \frac{9}{2} \frac{n^{7/2}}{Z(2E_{\rm IP})^{3/2}}.$$
 (1)

This semiempirical model for the polarization of an ion with the outermost electron having an ionization potential $E_{\rm IP}$ and principal quantum number n is shown for krypton in Fig. 2(b) as the ion charge state Q proceeds from the neutral atom to the bare Z=36 nucleus. With the increase in Q the larger force binding the electrons decreases the outer electron radius and polarizability. In addition to an inverse relationship between α and Q, large changes occur at the shell gaps (Q=8,26,34), where the radial expectation value of the bound-state electron decreases abruptly. As the ion states span from Kr to Kr³⁵⁺, the polarizability changes by a factor of 10^6 . It is interesting to note that, while the ADK formulation has yielded excellent agreement with experiments, it does not include the physics of field polarizability or the Stark shift of the binding energy.

In this work, we calculate the electron wave function of highly charged ions in ultrastrong fields. This is done to obtain insight into the electron wave-function polarization and Starkshifted bound-state energies. We demonstrate the impact of these field-induced changes to determine the ionization rates at intensities created with modern ultrahigh-intensity laser facilities. Our study concludes by demonstrating the generalization of the wave-function polarization for highly charged ions in ultrastrong laser fields using a scaling relationship between species.

II. THEORY

Our model approximates the atomic response as a "frozen" ion core with an "active," least tightly bound outermost electron interacting with an external field $(\vec{E} \cdot \vec{r} = |\vec{E}|z)$, nucleus, and ion core $V_{\rm core}(\vec{r})$. The Hartree approximation [35] is used for electron correlation. By way of example, the calculated ion-core potentials, bound states, and radially dependent effective charge for ${\rm Kr}^{25+}$ are shown in Fig. 3. The core-state radial probabilities in Fig. 3(a), which are consistent with [36], are offset to correspond to the binding energy in the potentials as an aid to the reader's eye. The electron correlation energy is included in Fig. 3(a). As shown by the radially dependent effective charge for ${\rm Kr}^{25+}$, core screening is involved for $r<0.25a_0$. By making a comparison to Fig. 1, where the peak value of $\psi^*(z)\psi(z)$ is at $0.4a_0$, one can see a significant fraction of the outermost electron penetrates the core.

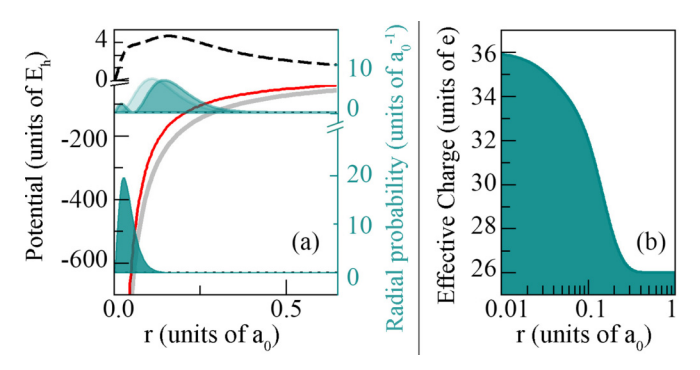


FIG. 3. (a) Potential energy for the ion core $Kr[1s^22s^22p^6]$ (left axis) including the Kr^{36+} Coulomb potential (gray thick line); the ion core potential $V_{\rm core}(\vec{r})$ (red solid line), which asymptotically is Kr^{26+} ; and the electron correlation energy for the core (black dashed line). A split scale is used in (a) for electron correlation energy. The radial probabilities, right axis in (a), for the electron core states (green shading) are offset according to binding energy. (b) The ion core is displayed as the radially dependent effective charge.

Using the quasistatic approximation, the Schrödinger equation for electron states of a highly charged ion is numerically solved in a hydrogenic basis set for the electron states in an external electric field [35]. The wave function for the outermost electron is used to determine the polarization and energy shift in the field. The interaction for each species ranges typically from a field strength of $0.1 \times BSI$ (0.01 of the BSI intensity) to $0.9 \times BSI$. In this range, the energy and dipole of the outermost electron wave function converge with a basis set of n = 25 for the principal quantum number. The field-free ionization energy of the calculated bound states typically ranges within $\sim 10\%$ of NIST values [37].

Intensities up to 10^{22} W cm⁻² are considered, which are well into the relativistic regime when the electron is in the continuum [8]. This occurs as the photoelectron gains energy as it is accelerated and displaced from the parent ion; in Fig. 1(b) the photoelectron will not reach a kinetic energy of $100E_h$ from the $12.4E_he^{-1}a_0^{-1}\hat{z}$ field until $z=-11a_0$.

The role of relativistic effects and the external laser magnetic field for the bound states of highly charged ions have been examined with semiclassical [11] and quantum [38] treatments. Including the external laser magnetic field in calculations changes the bound-state energy by a few percent at 10^{22} W cm⁻². For reference, the Zeeman energy from the laser magnetic field acting on the calculated polarized states is given in Fig. 4(a) relative to the Stark shift and bound-state energy.

For tunneling ionization, the angular distribution of the bound electron wave function as it appears in the continuum [39] from under the barrier [40] is deflected by \sim 0.1 rad at intensities above 10^{22} W cm $^{-2}$. This amount is negligible relative to changes in the angular distributions due to the Lorentz force for the photoelectron in the continuum [41]. Despite changes to the angle-resolved photoionization current, the magnetic field does not significantly affect the total ionization rate [11,42] up to intensities of 10^{22} W cm $^{-2}$.

The energies for the bound states we consider are <2.5% of the electron rest mass. As a result, the kinetic-energy, relativistic-energy, fine-structure shift is neglected. Due to the

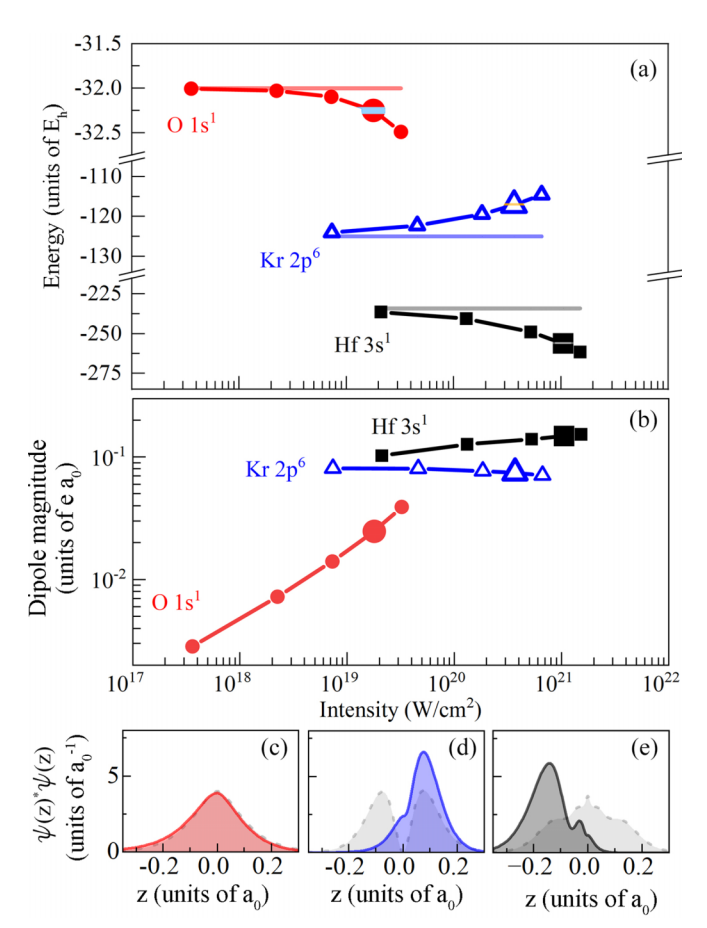


FIG. 4. (a) Binding energy for the outermost electrons of O⁷⁺ (dark red line and solid circles), Kr²⁶⁺ (dark blue line and open triangles), and Hf 61+ (black line and solid squares), labeled by the assignments O 1 s^1 , Kr 2 p^6 , and Hf 3 s^1 , respectively. As an aid to the eve the field-free binding energy is indicated as a light horizontal in each case. (b) The dipole magnitude for the outermost electrons for O⁷⁺ (red solid circles), Kr²⁶⁺ (blue open triangles), and Hf⁶¹⁺ (black, solid squares) is shown as a function of intensity. A larger symbol is used for the 0.71 BSI point, which is the field used in (c)–(e). $\psi(z)^*\psi(z)$ for the outermost electron are shown for (c) O⁷⁺ at a field of $22.6E_he^{-1}a_0^{-1}$ (red solid line and shading), (d) Kr²⁶⁺ at $102.5E_he^{-1}a_0^{-1}$ (blue solid line and shading), and (e) Hf ⁶¹⁺ at $173E_he^{-1}a_0^{-1}$ (black solid line and dark gray shading). The field-free $\psi(z)^*\psi(z)$ are also shown in (c)–(e) for reference (gray dashed line and light gray shading). The extent of the Zeeman energy splittings $(0.08E_h \text{ for } O^{7+}, 0.6E_h \text{ for } Kr^{26+}, \text{ and } 1.1E_h \text{ for } Hf^{61+}, \text{ which is }$ smaller than the symbol size) is indicated by a highlighted horizontal bar ΔE_h region within the 0.71 BSI Stark shift symbols in (a).

weakness of the atomic magnetic field relative to the laser magnetic field, we also neglect spin-orbit coupling.

Extensions of our work to highly charged ions with intensities above 10²² W cm⁻² [42,43] will need to involve careful consideration of the nonrelativistic approximation and role of the external laser magnetic field as well as the linear or circular external-field polarization [44].

III. POLARIZATION AND STARK SHIFT

An analysis of the outermost electron properties for O^{7+} , Kr^{26+} , and Hf^{61+} is presented in this section. The field-free

orbital descriptions for these species are O $1s^1$, Kr $1s^22s^22p^6$, and Hf $1s^22s^22p^63s^1$. These three cases were chosen because they demonstrate key characteristics of the response. Additional cases are given in the Appendix.

The calculated field-free binding energy and Stark-shifted binding energy of the outermost electron for O^{7+} , Kr^{26+} , and Hf^{61+} are plotted in Fig. 4(a). Depending on the orientation of the electron state, $\vec{p} \cdot \vec{E}$ can increase the ionization energy as the state becomes more tightly bound (more negative binding energies). This is the case for O^{7+} and Hf^{61+} when the induced dipole is parallel to the field. Conversely, the dipole of the outermost electron in Kr^{26+} has an antiparallel alignment. This lifts the energy of the state in the field, decreasing the ionization energy [45]. The magnitudes of the outermost-electron dipoles for O^{7+} , Kr^{26+} , and Hf^{61+} are shown in Fig. 4(b). The alignment of the electron probability $\psi^*(z)\psi(z)$ at an external field of $0.71 \times BSI$ can be compared to the field-free solution in Figs. 4(c)–4(e).

We begin with O⁷⁺ at an intensity of 10^{17} W cm⁻². The binding energy shifts in the field from $-32E_h$ to $-32.5E_h$ approaching the BSI intensity. The small induced dipole is due to the slight polarizability of the n = 1 state foreshadowed by the weak-field homogeneous polarizability model in Fig. 2(b). The $2.5 \times 10^{-2}ea_0$ dipole response at one half of the BSI intensity is barely observable in Fig. 4(c) as a $-0.025\hat{z}a_0$ shift of $\psi^*(z)\psi(z)$ from the field-free probability.

Turning next to Hf ⁶¹⁺, Fig. 4(a) portrays the bindingenergy changes from the field-free value of $-234~E_h$ to $-262~E_h$ as one approaches the BSI intensity at $2 \times 10^{21}~\rm W~cm^{-2}$. The induced dipole is of the order of $10^{-1}ea_0$ due to a combination of the larger radial values for the n=3state and the extremely high intensity. The peak value of $\psi^*(z)\psi(z)$ for the outermost electron in a field strength of $\sim 173E_he^{-1}a_0^{-1}$ is seen in Fig. 4(e) to be approximately $0.15a_0$ along $-\hat{z}$.

The Stark effect gives a splitting of the energy levels by mixing the atomic states and then interacting with the resulting electric dipole moments [46]. States shifting to lower energies, such as for O⁷⁺ and Hf ⁶¹⁺, result from an alignment with the field. Kr²⁶⁺ illustrates the impact of the external laser field on states shifting to higher energies due to an alignment opposite to the field. In terms of $|nlm\rangle$ states $|200\rangle$, $|210\rangle$, $|21-1\rangle$, and $|211\rangle$ in an electric field mix to create eigenstates with a dipole moment parallel and antiparallel to a \hat{z} field: $1/\sqrt{2} (|200\rangle - |210\rangle)$ and $1/\sqrt{2} (|200\rangle + |210\rangle)$. This high-energy state of the Stark-shifted manifold has its binding energy shifted by $\vec{p} \cdot \vec{E}$ up from the field-free value of $-125E_h$ to the value of $-115E_h$ shown in Fig. 4(a). The external field forces the electron in the direction of $-\hat{z}$, pushing back the initial alignment along \hat{z} ; the initial $0.08ea_0$ dipole at 10^{19} W cm⁻² drops to $0.07ea_0$ as one approaches 10^{21} W cm⁻². $\psi^*(z)\psi(z)$ for the outermost Kr $^{26+}$ electron is shown in Fig. 4(d).

IV. TUNNELING IONIZATION

Polarization and Stark shifts change the ionization response of the atom in an ultraintense laser. The polarization of the bound state, for example, with O⁷⁺, Kr²⁵⁺, and Hf ⁶¹⁺, shows an electron displacement toward the tunneling barrier

(see Fig. 1). The additional electron probability at the barrier increases the tunneling rate. As the tunneling-ionization rate is known to be an exponential function of the height of the barrier, Stark energy shifts also affect $E_{\rm IP}$ and the ionization rate.

Many experiments and theory models with atoms and molecules in strong and ultrastrong fields rely on tunneling ionization [47]. Atomic ionization rates are used to calibrate the peak field of high-intensity lasers [4]; an error in ionization rates can lead to a systemic error in the reported peak intensity for experiments. In this section, we focus on ionization by considering tunneling with and without the polarizability and Stark shift of the wave function. We also compare our rates to a widely used [25,48–53] ADK model of tunneling ionization.

The tunneling-ionization rate for a state may be obtained from the ionization probability current [54]. The probability current gives the tunneling-ionization rate W, which for hydrogenlike systems takes the form [54]

$$W = \frac{|B|^2}{2^{|m|}|m|!} \frac{1}{\kappa^{(\frac{2Q}{\kappa}-1)}} \left(\frac{2\kappa^3}{|\vec{E}|}\right)^{(\frac{2Q}{\kappa}-|m|-1)} \exp^{-(\frac{2\kappa^3}{3|\vec{E}|})}, \quad (2)$$

where $\kappa = \sqrt{2E_{\rm IP}}$ and B is determined by matching the quantum-mechanical wave function of the ionizing bound state to the asymptotic radial form ψ_c , given by

$$\psi_c(r) = Dr^{(Q/\kappa)-1}e^{-\kappa r},\tag{3}$$

$$D = B \times (-1)^{-(m+|m|)/2} \sqrt{\frac{2}{2l+1} \frac{(l-|m|)!}{(l+|m|)!}}.$$
 (4)

D and *B* are normalization constants only known in analytical form for the one-electron Coulomb problem.

Ammosov, Delone, and Krainov derived an analytical expression [33,54,55] for D using an effective quantum number $n^* = Q/\sqrt{2E_{\rm IP}}$. The resulting ionization rate is known as the complex atom-tunneling rate $W_{\rm ADK}$,

 $W_{\rm ADK}(|E|)$

$$= C_{n^*l^*}^2 E_{\text{IP}} \frac{(2l+1)(l+|m|)!}{2^{|m|}(|m|)!(l-|m|)!} \left(\frac{2(2E_{\text{IP}})^{3/2}}{|\vec{E}|}\right)^{2n^*-|m|-1} \times \exp\left(-\frac{2(2E_{\text{IP}})^{3/2}}{3|\vec{E}|}\right), \tag{5}$$

where $C_{n^*l^*}^2$ is given by

$$C_{n^*l^*}^2 = \frac{2^{2n^*}}{n^*\Gamma(n^* + l^* + 1)\Gamma(n^* - 1)}$$
 (6)

and $\Gamma(x)$ is the gamma function of x, $l^* = n_0^* - 1$, and n_0^* represents the effective principal quantum number of the lowest state with the given quantum number l. As mentioned, the complex-atom ADK model does not take into account the polarization of the electron wave function by the laser field or the Stark shift.

Our analysis uses the calculated wave function at the barrier to match the asymptotic tunneling wave function (3). This fitting is done at the inner classical turning point of the barrier (e.g., $z \approx -0.75a_0$ in Fig. 1) to obtain D. We include the Stark shift in the ionization rate by modifying the ionization potential and replacing it with the intensity-dependent

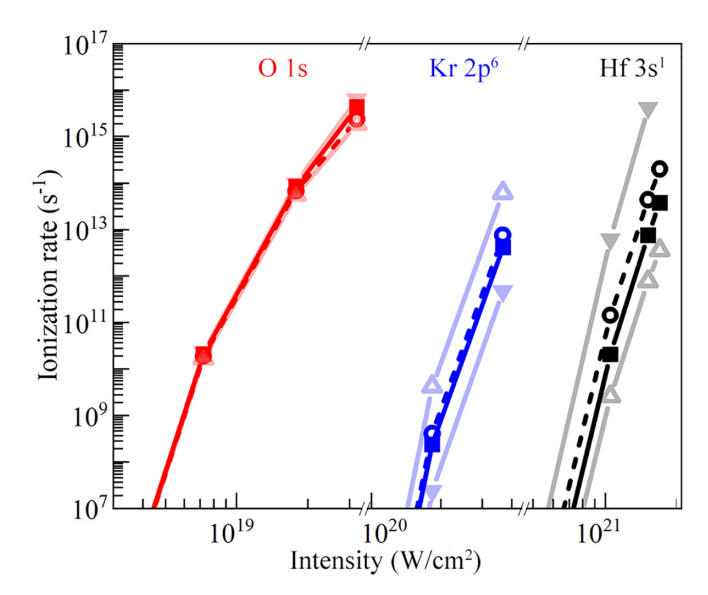


FIG. 5. Intensity-dependent ionization rates for O^{7+} (red, left), Kr^{26+} (blue, middle), and Hf^{61+} (black, right), labeled above the curves by the assignments O 1s, Kr 2 p^6 , and Hf 3 s^1 , respectively. Four tunneling-rate calculations are displayed under the conditions: field-polarized wave function with the field-free ionization energy (inverted solid triangles and light line); field-free wave function with the Stark-shifted ionization energy (open triangles and light line); field-polarized and Stark-shifted ionization energy (solid squares and dark solid line); and ADK (open circles and dashed line).

binding energy. Fitting the coefficients in ψ_c to the polarized wave-function solution addresses the change in the probability of the bound state at the tunneling barrier. Stark shifts are incorporated via $E_{\rm IP}$ in Eq. (2).

Our tunneling discussion begins with the response of O^{7+} at 10^{19} W cm⁻². The ionization curves are noted in Fig. 5 by the field-free orbital description O $1s^1$. The tunneling-ionization rate is plotted from 10^7 s⁻¹ to its highest point at $0.9 \times BSI$ field. In keeping with the smaller polarization and Stark shift for O^{7+} , we do not find the O^{7+} tunneling rate to be strongly affected by including the polarization or Stark shift. At the highest field, the polarization shift toward the barrier increases the ionization, and the shifted ionization energy decreases the tunneling rate. These counteracting effects in the tunneling change the rate by a negligible amount for rates $<10^{10}$ s⁻¹ and by a factor of 3 as the ionization rate approaches 10^{16} s⁻¹ at BSI. In addition, our results agree with the ADK rate, deviating only slightly as one approaches BSI, which is arguably expected for a hydrogenlike 1s response.

Proceeding next to Hf $^{61+}$, the ionization rate curve is noted in Fig. 5 by Hf $3s^1$. Considering only the $0.2ea_0$ polarization of the wave function toward the barrier [see Fig. 4(e)] gives a tunneling rate of $5 \times 10^{15} \, \mathrm{s}^{-1}$, which is 50 times higher than the ADK rate of $1 \times 10^{14} \, \mathrm{s}^{-1}$ near the BSI intensity of $2 \times 10^{21} \, \mathrm{W \, cm}^{-2}$. Including only the Stark shift (magnitude of $28E_h$) gives a rate of $4 \times 10^{12} \, \mathrm{s}^{-1}$. Accounting for both the polarization and Stark shift gives an offsetting result; near BSI the rate including both polarization and the Stark shift is $4 \times 10^{13} \, \mathrm{s}^{-1}$, which differs from the field-free ADK rate of $2 \times 10^{14} \, \mathrm{s}^{-1}$ by a factor of 5. In terms of the potential impact

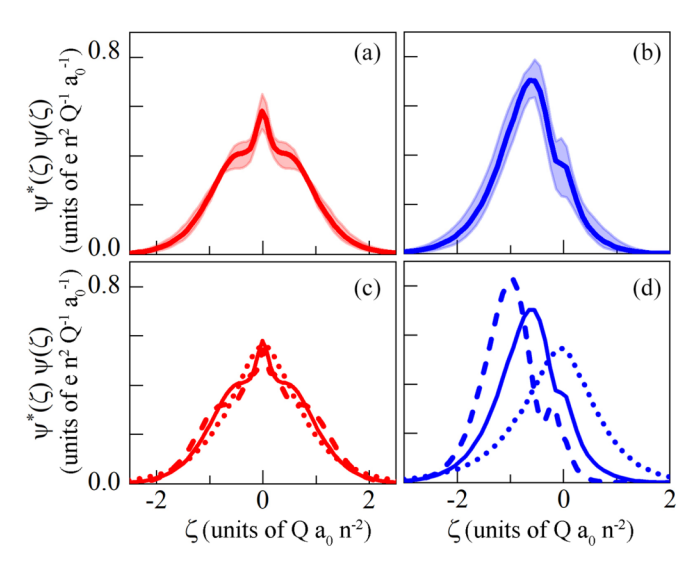


FIG. 6. Average of the scaled wave-function probability $\psi^*(\zeta)\psi(\zeta)$ (thick line) for the outermost electrons of C^{3+} , Ne^{6+} , Ar^{14+} , and Xe^{51+} (a) for no field and (b) in a field of $0.71 \times BSI$. The minimum and maximum $\psi^*(\zeta)\psi(\zeta)$ values across the species are indicated by shading. The average $\psi^*(\zeta)\psi(\zeta)$ (c) for no field and (d) at $0.71 \times BSI$ for the outermost electrons of the n=1 ions Ar^{16+} , Be^{2+} , and O^{7+} (dotted line); n=2 ions C^{3+} , Ne^{6+} , Ar^{14+} , and Xe^{51+} (solid line); and n=3 ions Kr^{25+} , Hf^{61+} , and U^{80+} (dashed line).

on the experimental measurements, a factor of 5 change in the rate for Hf $^{61+}$ at 10^{21} W cm $^{-2}$ corresponds to an $\sim 20\%$ change in the intensity. This change in the intensity is comparable to the best calibrations for high-intensity lasers [56,57].

The last species shown in Fig. 5 is Kr^{25+} ($\mathrm{Kr}\,2p^6$). Consistent with Hf $^{61+}$, we observe the impacts of the polarization and Stark shift largely cancel each other, giving a rate that is within a factor of 2 as one approaches the BSI at 3×10^{20} W cm⁻². However, the filled shell results in the outermost electron having an antiparallel dipole and Stark shift that decreases the ionization energy E_{IP} . The wave function in the field is polarized away from the tunneling barrier. As a result, tunneling is significantly lower due to reduced probability near the tunneling barrier. Overall, the Stark shift of E_{IP} is sufficient to raise the electron in the effective potential (decreasing the tunneling barrier height), so the rate increase

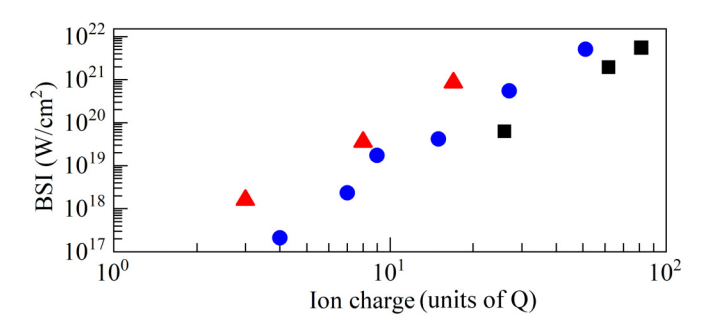


FIG. 7. Peak intensity (BSI) for the species calculated as a function of binding ion charge Q. The principal quantum number is indicated by the symbol color: n = 1, red triangles; n = 2, blue circles; and n = 3, black, squares.

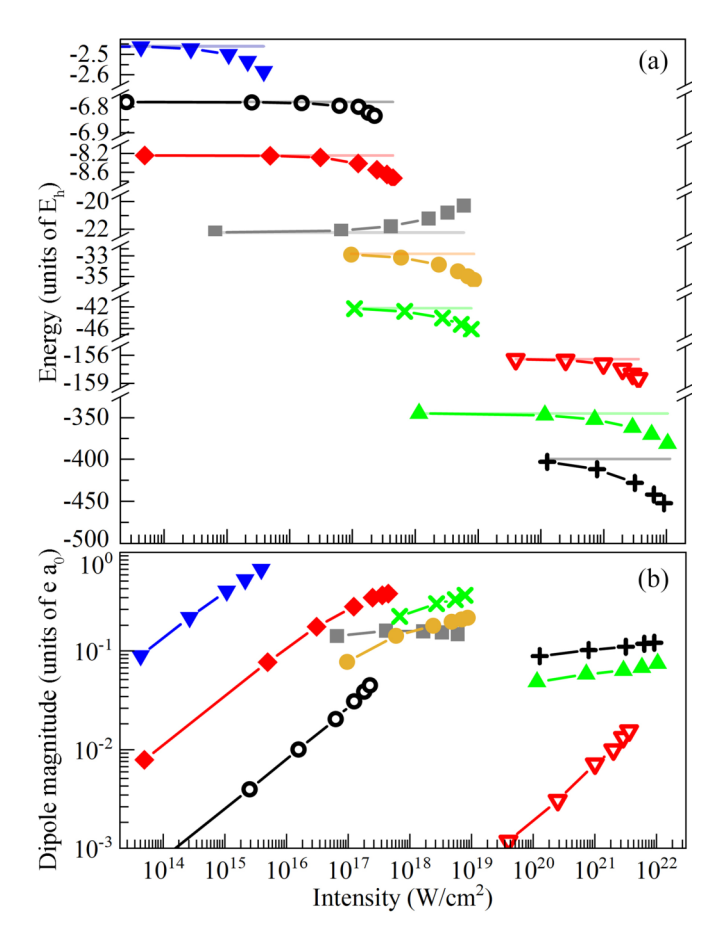


FIG. 8. (a) Stark-shifted binding energy and (b) magnitude of the dipole moment for the outermost electron as a function of the laser intensity for C^{3+} (blue solid inverted triangles), Be^{2+} (black open circles), Ne^{6+} (red solid diamonds), Ar^{9+} (gray solid squares), Ar^{14+} (dark yellow solid circles), Kr^{25+} (green crosses), Ar^{16+} (red open inverted triangles), Xe^{51+} (green solid triangles), and U^{80+} (black pluses).

from the Stark shift is comparable to the reduction from the amount of the wave function at the barrier.

Across multiple species included in the Appendix, we find an isolated consideration of the wave-function polarization or Stark shift can change the ionization rate by up to two orders of magnitude. However, in all cases, these offsets in the rate counteract within a typical factor of 2 to 5. The achieved experimental intensity for studies using an ADK rate calibration would need to be adjusted by between 5% and 20%. We add there may be other techniques [56–59] to calibrate ultrahigh-field experiments that could employ the Stark shift [60].

V. SCALING OF THE RESPONSE

In this section, we present the calculated high-field states in a scaled distance unit $\vec{\zeta} \equiv \frac{Qz}{n^2}\hat{z}$, which is based on the Bohr model. Figure 6 shows the electron probability for the outermost electron as a function of ζ for a variety of highly charged ions. For simplicity, we have limited the consideration here to s states.

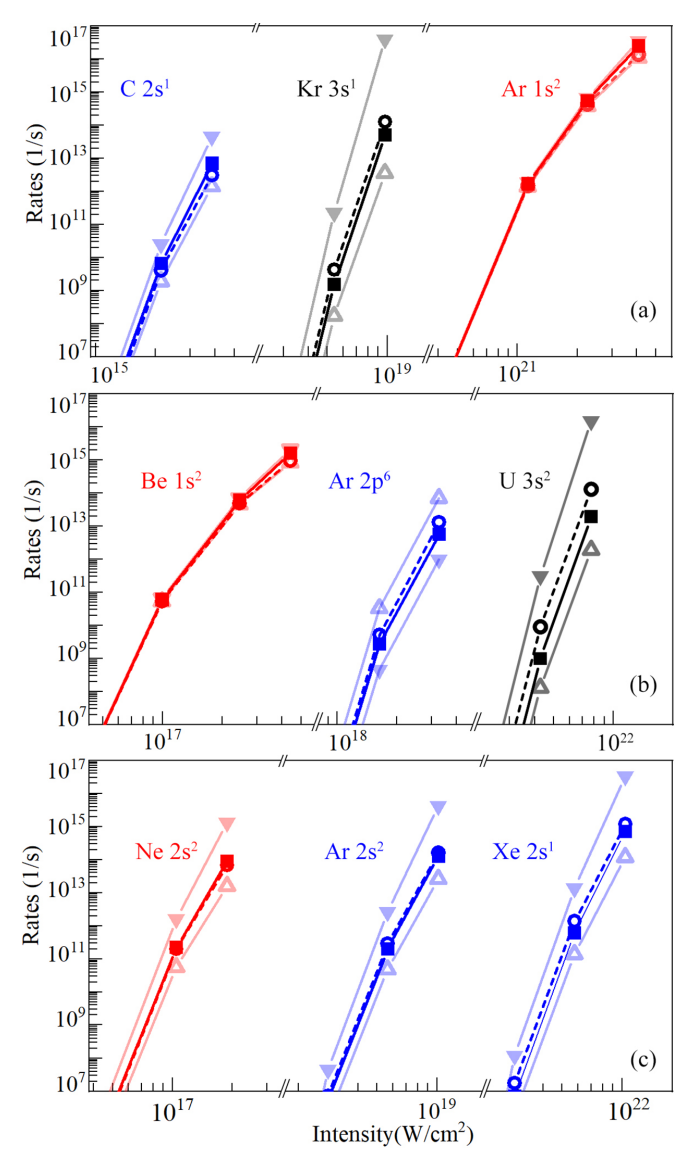


FIG. 9. Intensity-dependent tunneling-ionization rates of (a) C^{3+} (left), Kr^{25+} (middle), and Ar^{16+} (right); (b) Be^{3+} (left), Ar^{9+} (middle), and U^{80+} (right); and (c) Ne^{6+} (left), Ar^{14+} (middle), and Xe^{51+} (right). As an aid to the eye, the field-free orbital assignment is given above the corresponding curve. Four calculations are shown: the field-polarized wave function with the field-free ionization energy (inverted solid triangles and light line), field-free wave function with the Stark-shifted E_{IP} (open triangles and light line), polarized wave function with Stark-shifted E_{IP} (solid squares and dark line), and the ADK rate (open circles and dashed line).

Figure 6(a) shows the average $\psi^*(\zeta)\psi(\zeta)$ for n=2 species when the ions have no laser field, i.e., are field free. The minimum and maximum values for $\psi^*(\zeta)\psi(\zeta)$ across the species are indicated by shading around the average. These extreme values represent the differentiation between the states due to the outermost-electron state character and highly charged ion cores. One can see that when they are scaled, the differences in the field-free states are arguably small. $\psi^*(\zeta)\psi(\zeta)$ for these same n=2 states at a field of $0.7 \times BSI$ are shown in Fig. 6(b). One can see that the minimum and maximum extremes with the scaled polarized wave function

across C^{3+} to Xe^{51+} are only a factor of 2 to 3 larger than for the field-free case [Fig. 6(a)].

The inspection of $\psi^*(\zeta)\psi(\zeta)$ is extended to the n=1,2,3 states in Figs. 6(c) and 6(d). The average field-free wave functions for n=1,2,3 are graphed in Fig. 6(c). When the field-free electron probabilities for n=1,2,3 are expressed as $\psi^*(\zeta)\psi(\zeta)$, they are directly comparable; deviations due to the changes in the principal quantum number are not out of line with the changes in the wave function due to the various ion cores [Fig. 6(a)].

Finally, in an effort to generalize the polarizability and Stark shift we plot in Fig. 6(d) the average $\psi^*(\zeta)\psi(\zeta)$ for n=1,2,3 at a field of $0.7 \times BSI$ for each species. We note the BSI values for the species involved in the average range in intensity from 10^{15} to 10^{22} W cm⁻². The scaled dipoles for the average with $n=1,\ n=2,\ \text{and}\ n=3$ states are $-0.17ea_0Qn^{-2},\ -0.67ea_0Qn^{-2},\ \text{and}\ -1.01ea_0Qn^{-2},\ \text{respectively}$. Given the similarity of the scaled wave functions, the expectation value for the dipole moments as a function of the principal quantum number gives predictive power across the periodic table. By the way of example, we give the dipole from the scaled average $(p_{\text{scaled}} = \frac{n^2}{Q}p_\zeta)$: O^{7+} is $p_{\text{scaled}} = 0.021ea_0$, compared with the calculated $p=0.021ea_0$; Ar^{14+} is $p_{\text{scaled}} = 0.18ea_0$, compared with $p=0.20ea_0$; and Hf^{61+} is $p_{\text{scaled}} = 0.15ea_0$, compared with $p=0.15ea_0$.

VI. CONCLUSION

As matter interacts with ultrastrong fields, the bound electrons in ion states are both polarized and Stark shifted. The unprecedented range of laser intensities from 10^{15} to 10^{24} W cm⁻² can take the interaction from the neutral atom to a bare nucleus. We have used a single active electron approximation to calculate the polarization and Stark-shifted

binding energy of the outermost electron as a function of the external field strength. The calculated response with atoms from beryllium to uranium shows induced dipole and Stark shifts as significant as $0.1ea_0$ and $50E_h$. An application of the findings to tunneling revealed the change in the ionization rate due to the polarization of the wave function was countered by an offsetting change due to the Stark shift of the binding energy. The opposing roles of polarization and Stark shift resolve a long-standing question on how field-free derivations of the tunneling response have been successful in relativistic, ultrahigh-intensity experiments. When scaling with the ion charge and principal quantum number, the polarized wave functions reveal a common polarization response that can be used to predict the dipole moment for highly charged ions across the periodic table and intensity range from 1015 to $10^{22} \ \mathrm{W} \ \mathrm{cm}^{-2}$.

ACKNOWLEDGMENT

This material is based upon work supported by the National Science Foundation under Grants No. 2133728 and No. 2110462.

APPENDIX: COMPILATION OF POLARIZATION AND STARK SHIFT FOR HIGHLY CHARGED IONS

This Appendix provides a broader survey of results across the periodic table. Figure 7 gives a graphical summary of the species as a function of the ion core charge, peak interaction intensity, and principal quantum number. The Stark shift and magnitude of the laser-field-induced dipole moment for the species not displayed in Fig. 4 are included here in Fig. 8. Figure 9 is a compilation of the rates for species not included in the main text.

- [1] D. Strickland and G. Mourou, Compression of amplified chirped optical pulses, Opt. Commun. **56**, 219 (1985).
- [2] J. W. Yoon, Y. G. Kim, I. W. Choi, J. H. Sung, H. W. Lee, S. K. Lee, and C. H. Nam, Realization of laser intensity over 10²³ W/cm², Optica 8, 630 (2021).
- [3] International Committee on Ultrahigh Intensity Lasers, Intense laser labs world wide, www.icuil.org/activities/laser-labs.html.
- [4] K. Yamakawa, Y. Akahane, Y. Fukuda, M. Aoyama, J. Ma, N. Inoue, H. Ueda, and H. Kiriyama, Super strong field ionization of atoms by 10¹⁹ W cm⁻², 10 Hz laser pulses, J. Mod. Opt. 50, 2515 (2003).
- [5] N. Ekanayake, S. Luo, P. D. Grugan, W. B. Crosby, A. D. Camilo, C. V. McCowan, R. Scalzi, A. Tramontozzi, L. E. Howard, S. J. Wells, C. Mancuso, T. Stanev, M. F. Decamp, and B. C. Walker, Electron Shell Ionization of Atoms with Classical, Relativistic Scattering, Phys. Rev. Lett. 110, 203003 (2013).
- [6] M. Klaiber, E. Yakaboylu, C. Mueller, H. Bauke, G. G. Paulus, and K. Z. Hatsagortsyan, Spin dynamics in relativistic ionization with highly charged ions in super-strong laser fields, J. Phys. B 47, 065603 (2014).

- [7] M. W. Walser, D. J. Urbach, K. Z. Hatsagortsyan, S. X. Hu, and C. H. Keitel, Spin and radiation in intense laser fields, Phys. Rev. A 65, 043410 (2002).
- [8] M. Klaiber, K. Z. Hatsagortsyan, and C. H. Keitel, Above-threshold ionization beyond the dipole approximation, Phys. Rev. A 71, 033408 (2005).
- [9] M. Klaiber and K. Z. Hatsagortsyan, Spin-asymmetric laserdriven relativistic tunneling from p states, Phys. Rev. A 90, 063416 (2014).
- [10] M. Klaiber, E. Yakaboylu, and K. Z. Hatsagortsyan, Above-threshold ionization with highly charged ions in superstrong laser fields. I. Coulomb-corrected strong-field approximation, Phys. Rev. A 87, 023417 (2013).
- [11] P. D. Grugan, S. Luo, M. Videtto, C. Mancuso, and B. C. Walker, Classical study of ultrastrong nonperturbative-field interactions with a one-electron atom: Validity of the dipole approximation for the bound-state interaction, Phys. Rev. A 85, 053407 (2012).
- [12] R. R. Freeman, P. H. Bucksbaum, H. Milchberg, S. Darack, D. Schumacher, and M. E. Geusic, Above-Threshold Ionization with Subpicosecond Laser Pulses, Phys. Rev. Lett. 59, 1092 (1987).

- [13] P. Agostini, P. Breger, A. L'Huillier, H. G. Muller, G. Petite, A. Antonetti, and A. Migus, Giant Stark Shifts in Multiphoton Ionization, Phys. Rev. Lett. 63, 2208 (1989).
- [14] N. I. Shvetsov-Shilovski, D. Dimitrovski, and L. B. Madsen, Ionization in elliptically polarized pulses: Multielectron polarization effects and asymmetry of photoelectron momentum distributions, Phys. Rev. A 85, 023428 (2012).
- [15] W. Yang, J. Li, W. Jia, H. Zhang, X. Liu, M. Zhu, X. Song, and J. Chen, Effect of the Stark shift on the low-energy interference structure in strong-field ionization, Phys. Rev. A 103, 053105 (2021).
- [16] S. I. Themelis and C. A. Nicolaides, Field-induced tunneling rates, polarizabilities, and hyperpolarizabilities for low-lying excited-states of Li and Na, Phys. Rev. A **51**, 2801 (1995).
- [17] N. S. Koester, K. Kolata, R. Woscholski, C. Lange, G. Isella, D. Chrastina, H. von Kaenel, and S. Chatterjee, Giant dynamical Stark shift in germanium quantum wells, Appl. Phys. Lett. 98, 161103 (2011).
- [18] A. DiChiara, E. Chowdhury, G. Ongadi, B. Walker, and R. Tamosaitis, TEM₀₀ terawatt amplification by use of micro-optic spatial mode conversion, Opt. Lett. **28**, 2106 (2003).
- [19] B. C. Walker, C. Tóth, D. N. Fittinghoff, T. Guo, D.-E. Kim, C. Rose-Petruck, J. A. Squier, K. Yamakawa, K. R. Wilson, and C. P. J. Barty, A 50-EW/cm² Ti:sapphire laser system for studying relativistic light-matter interactions, Opt. Express 5, 196 (1999).
- [20] M. Perry, D. Pennington, B. Stuart, G. Tietbohl, J. Britten, C. Brown, S. Herman, B. Golick, M. Kartz, J. Miller, H. Powell, M. Vergino, and V. Yanovsky, Petawatt laser pulses, Opt. Lett. 24, 160 (1999).
- [21] E. A. Chowdhury, C. P. J. Barty, and B. C. Walker, "Non-relativistic" ionization of the L-shell states in argon by a "relativistic" 10^{19} W/cm² laser field, Phys. Rev. A **63**, 042712 (2001).
- [22] S. Palaniyappan, R. Mitchell, R. Sauer, I. Ghebregziabher, S. L. White, M. F. Decamp, and B. C. Walker, Ionization of Methane in Strong and Ultrastrong Relativistic Fields, Phys. Rev. Lett. 100, 183001 (2008).
- [23] S. Palaniyappan, A. DiChiara, I. Ghebregziabher, E. L. Huskins, A. Falkowski, D. Pajerowski, and B. C. Walker, Multielectron ultrastrong laser field ionization of Ar^{n+} , Kr^{m+} and Xe^{l+} ($n \le 9$, $m \le 9$, $l \le 12$) at intensities from 10^{15} W cm⁻² to 10^{18} W cm⁻², J. Phys. B **39**, S357 (2006).
- [24] A. D. DiChiara, I. Ghebregziabher, R. Sauer, J. Waesche, S. Palaniyappan, B. L. Wen, and B. C. Walker, Relativistic MeV Photoelectrons from the Single Atom Response of Argon to a 10¹⁹ W/cm² Laser Field, Phys. Rev. Lett. 101, 173002 (2008).
- [25] A. S. Kornev, E. B. Tulenko, and B. A. Zon, Multiple ionization of Ar, Kr, and Xe in a superstrong laser field, Phys. Rev. A 84, 053424 (2011).
- [26] B. Walker, B. Sheehy, L. F. DiMauro, P. Agostini, K. J. Schafer, and K. C. Kulander, Precision Measurement of Strong Field Double Ionization of Helium, Phys. Rev. Lett. 73, 1227 (1994).
- [27] S. Larochelle, A. Talebpour, and S. Chin, Non-sequential multiple ionization of rare gas atoms in a Ti: sapphire laser field, J. Phys. B **31**, 1201 (1998).
- [28] P. B. Corkum, Plasma Perspective on Strong Field Multiphoton Ionization, Phys. Rev. Lett. 71, 1994 (1993).
- [29] W. Becker, F. Grasbon, R. Kopold, D. B. Milošević, G. G. Paulus, H. Walther, Above-threshold ionization: From classical

- features to quantum effects, Adv. At., Mol., Opt. Phys. 48, 35 (2002).
- [30] P. Eckle, A. N. Pfeiffer, C. Cirelli, A. Staudte, R. Doerner, H. G. Muller, M. Buettiker, and U. Keller, Attosecond ionization and tunneling delay time measurements in helium, Science 322, 1525 (2008).
- [31] A. S. Landsman, M. Weger, J. Maurer, R. Boge, A. Ludwig, S. Heuser, C. Cirelli, L. Gallmann, and U. Keller, Ultrafast resolution of tunneling delay time, Optica 1, 343 (2014).
- [32] U. S. Sainadh, H. Xu, X. Wang, A. Atia-Tul-Noor, W. C. Wallace, N. Douguet, A. Bray, I. Ivanov, K. Bartschat, A. Kheifets, R. T. Sang, and I. V. Litvinyuk, Attosecond angular streaking and tunnelling time in atomic hydrogen, Nature (London) 568, 75 (2019).
- [33] M. V. Ammosov, Tunnel ionization of complex atoms and of atomic ions in an alternating electromagnetic field, Sov. Phys. JETP **64**, 1191 (1987).
- [34] D. Ghosh and B. Raka, Theoretical calculation of absolute radii of atoms and ions. Part 1. The atomic radii, Int. J. Mol. Sci. 3, 87 (2002).
- [35] J. Izaac and J. Wang, Computational Quantum Mechanics (Springer, Cham, 2018).
- [36] F. Salvat, A. Jablonski, and C. Powell, Elsepa-Dirac partial-wave calculation of elastic scattering of electrons and positrons by atoms, positive ions and molecules, Comput. Phys. Commun. 165, 157 (2005).
- [37] A. Kramida, Yu. Ralchenko, J. Reader, and NIST ASD Team, NIST Atomic Spectra Database, version 5.9, https://physics. nist.gov/asd.
- [38] H. Bauke, H. G. Hetzheim, G. R. Mocken, M. Ruf, and C. H. Keitel, Relativistic ionization characteristics of laser-driven hydrogenlike ions, Phys. Rev. A 83, 063414 (2011).
- [39] J. Peatross, C. Mueller, and C. H. Keitel, Electron wave-packet dynamics in a relativistic electromagnetic field: 3-d analytical approximation, Opt. Express 15, 6053 (2007).
- [40] M. Klaiber, E. Yakaboylu, H. Bauke, K. Z. Hatsagortsyan, and C. H. Keitel, Under-the-Barrier Dynamics in Laser-Induced Relativistic Tunneling, Phys. Rev. Lett. 110, 153004 (2013).
- [41] S. Palaniyappan, I. Ghebregziabher, A. DiChiara, J. MacDonald, and B. C. Walker, Emergence from nonrelativistic strong-field rescattering to ultrastrong-field laser-atom physics: A semiclassical analysis, Phys. Rev. A 74, 033403 (2006).
- [42] N. Milosevic, V. Krainov, and T. Brabec, Relativistic theory of tunnel ionization, J. Phys. B 35, 3515 (2002).
- [43] M. Klaiber, K. Z. Hatsagortsyan, and C. H. Keitel, Fully relativistic laser-induced ionization and recollision processes, Phys. Rev. A 75, 063413 (2007).
- [44] S. S. Luo, P. D. Grugan, and B. C. Walker, Classical study of atomic bound state dynamics in circularly polarized ultrastrong fields, J. Phys. B 47, 135601 (2014).
- [45] N. Zettili, Quantum Mechanics: Concepts and Applications (Wiley, Hoboken, NJ, 2009).
- [46] N. Delone and V. Krainov, AC-Stark shift of atomic levels, Usp. Fiz. Nauk 169, 753 (1999).
- [47] T. Otobe, K. Yabana, and J. I. Iwata, First-principles calculations for the tunnel ionization rate of atoms and molecules, Phys. Rev. A **69**, 053404 (2004).
- [48] A. Yandow, T. Toncian, and T. Ditmire, Direct laser ion acceleration and above-threshold ionization at intensities from 10^{21} W/cm² to 3×10^{23} W/cm², Phys. Rev. A **100**, 053406 (2019).

- [49] K. Yamakawa, Y. Akahane, Y. Fukuda, M. Aoyama, N. Inoue, H. Ueda, and T. Utsumi, Many-Electron Dynamics of a Xe Atom in Strong and Superstrong Laser Fields, Phys. Rev. Lett. 92, 123001 (2004).
- [50] E. Murakami, R. Mizoguchi, Y. Yoshida, A. Kitashoji, N. Nakashima, and T. Yatsuhashi, Multiple strong field ionization of metallocenes: Applicability of ADK rates to the production of multiply charged transition metal (Cr, Fe, Ni, Ru, Os) cations, J. Photochem. Photobiol., A 369, 16 (2019).
- [51] P. Wustelt, M. Möller, T. Rathje, A. M. Sayler, T. Stöhlker, and G. G. Paulus, Momentum-resolved study of the saturation intensity in multiple ionization, Phys. Rev. A 91, 031401(R) (2015).
- [52] V. M. Ristic and J. M. Stevanovic, Atom charge states, z and comparing the ADK and CADK-theories, Laser Phys. 19, 989 (2009).
- [53] E. Gubbini, U. Eichmann, M. Kalashnikov, and W. Sandner, Core Relaxation in Atomic Ultrastrong Laser Field Ionization, Phys. Rev. Lett. 94, 053602 (2005).
- [54] C. Bisgaard and L. Madsen, Tunneling ionization of atoms, Am. J. Phys. 72, 249 (2004).
- [55] M. Ammosov, N. Delone, and V. Krainov, Tunnel ionization of complex atoms and atomic ions in a varying electromagneticfield, Zh. Eksp. Teor. Fiz. 91, 2008 (1986).

- [56] C. Z. He, A. Longman, J. A. Perez-Hernandez, M. de Marco, C. Salgado, G. Zeraouli, G. Gatti, L. Roso, R. Fedosejevs, and W. T. Hill, Towards an in situ, full-power gauge of the focal-volume intensity of petawatt-class lasers, Opt. Express 27, 30020 (2019).
- [57] M. Kalashnikov, A. Andreev, K. Ivanov, A. Galkin, V. Korobkin, M. Romanovsky, O. Shiryaev, M. Schnuerer, J. Braenzel, and V. Trofimov, Diagnostics of peak laser intensity based on the measurement of energy of electrons emitted from laser focal region, Laser Part. Beams 33, 361 (2015)
- [58] K. A. Ivanov, I. N. Tsymbalov, O. E. Vais, S. G. Bochkarev, R. V. Volkov, V. Y. Bychenkov, and A. B. Savel'ev, Accelerated electrons for in situ peak intensity monitoring of tightly focused femtosecond laser radiation at high intensities, Plasma Phys. Controlled Fusion 60, 105011 (2018).
- [59] K. A. Ivanov, I. N. Tsymbalov, A. V. Rusakov, R. V. Volkov, and A. B. Savel'ev, High energy electrons accelerated in the field of tightly focused relativistic laser pulse for peak intensity evaluation, J. Phys.: Conf. Ser. 941, 012046 (2017).
- [60] G. D. Stevens, C.-H. Iu, T. Bergman, H. J. Metcalf, I. Seipp, K. T. Taylor, and D. Delande, Absolute Calibration of Electric Fields Using Stark Spectroscopy, Phys. Rev. Lett. 75, 3402 (1995).